Geochemical Perspectives Letters

No V-Fe-Zn isotopic variation in basalts from the 2021 Fagradalsfjall eruption

M.A. Stow, J. Prytulak, K.W. Burton, G.M. Nowell, E.W. Marshall, S.A. Halldórsson, S. Matthews, M.B. Rasmussen, E. Ranta, A. Caracciolo

Supplementary Information

The Supplementary Information includes:

1. Analytical Methods

Chemical purification and isotopic analysis were performed at the Arthur Holmes Isotope Geology Laboratory, Durham University.

Sample Digestion

Whole rock samples were ground into homogeneous powders by hand using an agate pestle and mortar, which was cleaned with low-Fe quartz sand between samples to avoid contamination. Approximately 30–50 mg of each powder was digested in 3 mL Teflon Distilled (TD) 29 M HF and 1 mL TD 16 M HNO_3 on a hotplate at 160 °C for 48 hours. Samples were evaporated at 120 °C to incipient dryness, then the residues were repeatedly covered with TD 16 M HNO_3 and evaporated at 180 °C until dark brown, indicating that insoluble fluorides were destroyed. Samples were dissolved in 1 mL TD 6 M HCl for the first column chromatography procedure.

Column Chromatography

The following column chromatography procedure quantitatively separates V, Fe and Zn from the same sample digestion. The first column follows the method of Sossi *et al.* (2015). Samples were loaded in 1 mL TD 6 M HCl onto Savillex

PFA columns containing 2 mL of pre-cleaned Bio-Rad AG1-X8 resin (200–400 mesh). The V fraction was collected as the samples were loaded, and with a further 4 mL TD 6 M HCl. Vanadium was eluted with most other matrix elements at this stage, and four further column chromatography procedures were required to fully purify the V fraction. The V fraction was evaporated and the residue was covered with TD 16 M HNO_3 and evaporated at 160 °C. This step was carried out twice between every column procedure to destroy any organic resin which may have passed through the frits.

After a 10 mL TD 6 M HCl wash, Fe was collected in 6 mL TD 0.5 M HCl and Zn was collected in 4 mL TD 3 M HNO_3. The Zn fraction was processed through the entire column procedure a second time. The Fe and Zn fractions were then evaporated and dissolved in 1 mL TD 3 % HNO_3 for isotopic analysis.

The procedure for further V separation is adapted from Nielsen *et al.* (2011) and Wu *et al.* (2016). The underlying principle is that V^{5+} forms anionic V-peroxide complexes with hydrogen peroxide (H_2O_2) in mildly acidic solutions, and these complexes will partition strongly onto AG1-X8 resin (Nielsen *et al.*, 2011). However, before H_2O_2 can be used, all Fe and Ti must be removed, because Fe and Ti can catalyse the dissociation of H_2O_2 to water and oxygen (Nielsen *et al.*, 2011). The first column procedure separates Fe, and the second column procedure, from Wu *et al.* (2016), removes Ti. The third column procedure, from Nielsen *et al.* (2011) then uses H_2O_2 and separates V from remaining matrix elements.

Column 2 (Wu *et al.*, 2016) uses 2 mL of pre-cleaned AG50W-X12 cation resin (200–400 mesh) in Savillex PFA columns. Samples were loaded in 1 mL 1 M HNO_3. 4 mL TD 1 M HNO_3 + 0.1 M HF was used to elute Ti and Al. The V fraction was then collected in 20 mL TD 1.2 M HNO_3.

Column 3 (Nielsen *et al.*, 2011) uses 1 mL of pre-cleaned AG1-X8 resin in quartz glass columns. Samples were dissolved in 1 mL 0.01 M HCl, and 33 µL H_2O_2 (1 % v/v) was added to cool samples immediately before loading, to form the V-peroxide complexes which partition onto the resin. Most matrix elements were eluted with 21 mL TD 0.01 M HCl + 1 % v/v H_2O_2 and V was then collected with 8 mL TD 1 M HCl.

The final two columns, from Nielsen *et al.* (2011) are small-scale clean-up columns designed to remove all remaining Ti and Cr from samples, because ^{50}Ti and ^{50}Cr are direct interferences on the minor ^{50}V isotope (Nielsen *et al.*, 2011). These columns were typically repeated twice each, with a Cr clean-up column always being the final column before isotopic analysis. For both procedures, Teflon micro-columns containing 100 µL AG1-X8 resin were used.

For the Ti clean-up column, samples were loaded in 1 mL TD 2 M HF. Vanadium was collected as the sample was loaded, and with a further 1.2 mL TD 2 M HF and 1.4 mL TD 0.5 M HF/HCl mixture. For the Cr clean-up column, which is a scaled down version of column 3, samples were dissolved in 1 mL TD 0.01 M HCl and 33 µL H_2O_2 was added to cool samples immediately before loading. After a wash of 0.6 mL TD 0.01 M HCl + 1 % H_2O_2, V was collected in 0.8 mL TD 1 M HCl. Samples were then re-dissolved in TD 3 % HNO_3 for isotopic analysis.

Isotope Ratio Measurements

All isotope ratio measurements were undertaken on Neptune or NeptunePlus MC-ICP-MS at Durham University. The USGS reference material BIR-1a was processed alongside unknowns, and gave Fe, V and Zn isotopic compositions which agree with previous measurements.

Vanadium. Vanadium isotope ratio measurements were made in medium resolution mode ($m/\Delta m \approx 6000$–8000), which allows V to be resolved from isobaric interferences. The sample introduction system consisted of a PFA concentric flow nebuliser (uptake rate 50 µL/min) coupled to an Aridus 2 desolvating nebuliser system, giving typical sensitivity of >100 V/ppm on ^{51}V. 2 mL sample aliquots were diluted with TD 3 % HNO_3 to a concentration of 1 µg/g V. Masses ^{48}Ti, ^{49}Ti, ^{50}V, ^{51}V, ^{52}Cr and ^{53}Cr were measured in Faraday cups L4, L2, L1, C, H1 and H3 respectively, with a 10^{10} Ω resistor connected to the centre cup to measure signals >50 V on ^{51}V. Standard sample bracketing with the AA standard (Nielsen *et al.*, 2011) was used to correct for mass bias. ^{48}Ti, ^{49}Ti, ^{52}Cr and ^{53}Cr were used to correct for interferences of ^{50}Ti and ^{50}Cr on ^{50}V, using the exponential law ($R_T = R_M \times (m_1/m_2)^{\beta}$ .Two BDH solutions (Nielsen *et al.*, 2011) were doped with 100 ppb Ti and Cr, respectively, and measured during every sequence. The β factor was then varied iteratively until δ^{51}V matched the long-term average BDH value of approximately −1.19 ‰ to −1.23 ‰ (Nielsen

et al., 2011; Wu *et al.*, 2016). These β factors were then used to correct for the interferences of ^{50}Ti and ^{50}Cr on all samples in the sequence, after Wu *et al.* (2016). USGS reference material BIR-1a gave a $\delta^{51}V_{AA}$ value of −0.87 ± 0.03 ‰ (2 s.d., n = 3).

Iron. Iron isotope ratio measurements were made in medium resolution mode ($m/\Delta m$ ≈ 6000–8000), which allows Fe to be resolved from isobaric oxide and nitride interferences. The sample introduction system consisted of a Savillex CF50 concentric flow nebuliser and ESI SIS spray chamber, giving a sensitivity of 5–8 V/ppm on ^{56}Fe. 2 mL sample aliquots were diluted with TD 3 % HNO_3 to a concentration of 10 µg/g Fe, and doped with 8 µg/g Ni. Masses ^{53}Cr, ^{54}Fe, ^{56}Fe, ^{57}Fe, ^{60}Ni and ^{61}Ni were measured on Faraday cups L4, L2, L1, C, H2 and H4. A 10^{10} Ω resistor was connected to L1 to measure signals of >50 V on ^{56}Fe. The isobaric interference of ^{54}Cr on ^{54}Fe was corrected by monitoring ^{53}Cr and assuming an exponential law. A combination of standard sample bracketing and external element doping with Ni was used to correct for mass bias (*e.g.*, Gong *et al.*, 2020). Samples were bracketed using the IRMM-524 standard, which is isotopically indistinguishable from IRMM-014 (Craddock and Dauphas, 2011). USGS reference material BIR-1a gave a $\delta^{56}Fe_{IRMM\text{-}524}$ value of 0.065 ± 0.043 ‰ (2 s.d., n = 6).

Zinc. Zinc isotope ratio measurements were made in low resolution mode ($m/\Delta m$ ≈ 400). The sample introduction system consisted of a Savillex CF50 concentric flow nebuliser and ESI SIS spray chamber, giving typical sensitivity of 6–7 V/ppm on ^{64}Zn. 2 mL sample aliquots were diluted with TD 3 % HNO_3 to a concentration of 750 ng/g Zn, and doped with 375 ng/g Cu. Masses ^{62}Ni, ^{63}Cu, ^{64}Zn, ^{65}Cu, ^{66}Zn, ^{67}Zn and ^{68}Zn were measured in Faraday cups L3, L2, L1, C, H1, H2, and H3, and 10^{11} Ω resistors were used on all cups. The isobaric interference of ^{64}Ni on ^{64}Zn was corrected by monitoring ^{62}Ni and assuming an exponential law. A combination of standard sample bracketing with the AA-ETH Zn solution (Archer *et al.*, 2017) and external element doping with Cu was used to correct for mass bias. Data in this study is reported relative to AA-ETH, which is offset relative to the commonly used reference standard JMC Lyon (Maréchal *et al.*, 1999) by +0.28 ± 0.02 ‰ (Archer *et al.*, 2017). This correction can be used to recast the data in this study relative to JMC-Lyon. USGS reference material BIR-1a gave a $\delta^{66}Zn_{AA\text{-}ETH}$ value of −0.033 ± 0.010 ‰ (2 s.d., n = 3), which is equivalent to a $\delta^{66}Zn_{JMC\text{-}Lyon}$ value of +0.247 ± 0.010 ‰ (2 s.d., n = 3).

2. Results

Table S-1 Vanadium, iron and zinc isotopic compositions of Fagradalsfjall lavas. Errors are given as 2 standard deviations of at least three measurements of an individual sample. Sample names and eruption day are from Halldórsson *et al.* (2022), where the eruption day is the best estimate of the day the material was erupted from the vent. The eruption day for sample G20210404-1 is unknown, but is between days 4 and 11. This sample is plotted as day 8 in all figures, which is the midpoint of this time period. Zinc isotopic compositions are expressed relative to the AA-ETH standard (Archer *et al.*, 2017). Data is recast relative to the JMC-Lyon standard using the correction of +0.28 ‰ (Archer *et al.*, 2017).

Sample Name	Eruption Day	$\delta^{51}V_{AA}$ (‰)	2 s.d.	*n*	$\delta^{56}Fe_{IRMM-524}$ (‰)	2 s.d.	$\delta^{57}Fe_{IRMM-524}$ (‰)	2 s.d.	*n*	$\delta^{66}Zn_{AA-ETH}$ (‰)	$\delta^{66}Zn_{JMC-Lyon}$ (‰)	2 s.d.	$\delta^{67}Zn_{AA-ETH}$ (‰)	2 s.d.	*n*
G20210321-2	2	−0.95	0.09	5	0.068	0.053	0.108	0.086	3	−0.027	0.253	0.021	−0.059	0.027	3
G20210323-1	4	−0.89	0.05	3	0.081	0.041	0.116	0.051	3	−0.028	0.252	0.036	−0.074	0.029	3
G20210330-2	11	−0.86	0.03	3	0.052	0.020	0.086	0.050	3	−0.026	0.254	0.003	−0.052	0.050	3
G20210404-1	4–11	−0.89	0.04	3	0.055	0.027	0.089	0.048	3	−0.012	0.268	0.017	+0.002	0.047	3
G20210405-1	17	−0.86	0.06	3	0.082	0.018	0.108	0.029	3	−0.019	0.261	0.009	−0.024	0.013	3
G20210412-1	24	−0.87	0.04	3	0.065	0.040	0.096	0.045	5	−0.020	0.260	0.013	−0.038	0.048	3
G20210412-2	24	−0.88	0.07	3	0.059	0.060	0.106	0.089	5	+0.013	0.293	0.027	−0.013	0.078	3
G20210416-3	28	−0.85	0.07	3	0.047	0.042	0.086	0.075	3	−0.037	0.243	0.024	−0.066	0.043	3
G20210416-4	25	−0.90	0.06	3	0.094	0.049	0.135	0.059	6	−0.042	0.238	0.003	−0.058	0.087	3
G20210424-5	36	−0.86	0.07	3	0.060	0.013	0.093	0.048	4	−0.023	0.257	0.031	−0.028	0.031	3
BIR-1a		−0.87	0.03	3	0.065	0.043	0.085	0.067	6	−0.033	0.247	0.010	−0.078	0.049	3

Table S-2 Compilation of data from Halldórsson *et al.* (2022) presented in this study.

Sample Name	Eruption Day	TiO_2 (wt. %)	K_2O (wt. %)	K_2O/TiO_2	La (µg/g)	Yb (µg/g)	La/Yb	$^{206}Pb/^{204}Pb$	2 s.e. (Abs)	$^{87}Sr/^{86}Sr$	2 s.e. (Abs)	$^{143}Nd/^{144}Nd$	2 s.e. (Abs)
G20210321-2	2	0.96	0.136	0.142	4.3	1.99	2.16			0.703109	0.000005	0.513010	0.000003
G20210323-1	4	0.97	0.144	0.148	4.3	1.96	2.20	18.7328	0.0012	0.703108	0.000008	0.513017	0.000003
G20210330-2	11	1.01	0.194	0.192	5.1	1.89	2.68	18.7567	0.0013	0.703125	0.000007	0.512991	0.000003
G20210404-1	4–11	1.03	0.213	0.208						0.703157	0.000005	0.512972	0.000004
G20210405-1	17	1.01	0.193	0.191	6.4	2.26	2.81	18.7607	0.0019	0.703139	0.000006	0.512984	0.000003
G20210412-1	24	1.08	0.259	0.241	8.0	2.13	3.76	18.8229	0.0014	0.703183	0.000006	0.512949	0.000004
G20210412-2	24	1.08	0.263	0.243									
G20210416-3	28	1.04	0.236	0.227	7.0	2.00	3.51						
G20210416-4	25	1.08	0.266	0.246	7.5	1.94	3.88						
G20210424-5	36	1.10	0.282	0.256	8.3	2.04	4.05	18.8389	0.0016				

3. Correcting Fe Isotopes for Fractional Crystallisation

Many studies correct the Fe isotopic composition of basalts for the effect of olivine crystallisation, in order to determine the Fe isotopic composition of the primary magma at the time of mantle melting ($\delta^{56}Fe_{prim}$).

The method, first presented in Sossi *et al*. (2016), is a mass balance calculation where olivine (with a composition in equilibrium with the current melt), is progressively added back into the melt until a Mg# of 0.74 is reached. This is assumed to reflect the composition of a primary mantle derived magma. The resulting change in the Fe isotopic composition of the melt is then also calculated by a mass balance calculation, assuming an appropriate $\Delta^{56}Fe_{ol\text{-}melt}$ value.

For the calculation, the FeO, MgO and $Fe^{3+}/\Sigma Fe$ of the uncorrected basalt must be known (or assumed), and used to calculate an initial Mg# ($Mg\# = Mg^{2+}/(Mg^{2+} + Fe^{2+})$. The number of moles of Mg^{2+} and Fe^{2+} can be calculated using the atomic mass of MgO (40.3 amu) and FeO (71.8 amu) and the weight percent concentrations of MgO and FeO in the basalt (*i.e.* moles Mg^{2+} = MgO (wt. %)/40.3).

Following Sossi *et al*. (2016), for each 1 % incremental addition of olivine:

1) Calculate the composition of the olivine in equilibrium with the melt. We assume a Fe/Mg partition coefficient for olivine of 0.3 (Roeder and Emslie, 1970). Therefore, the Fe/Mg ratio of the olivine is given as:

$$\left(\frac{Fe}{Mg}\right)_{Ol} = K_{D\,Ol-melt}^{Fe-Mg} \times \left(\frac{Fe}{Mg}\right)_{melt}. \quad \text{(S-1)}$$

From olivine stoichiometry, we know that the number of moles of Fe + Mg must equal 2, which can be substituted into Equation S-1 to calculate the moles of Mg^{2+} and Fe^{2+} in the olivine. This can then be transformed into a concentration in wt. % using the atomic masses of the elements using Equations S-5 and S-7 as:

$$Fe^{2+} + Mg^{2+} = 2, \quad \text{(S-2)}$$

$$\left(\frac{Fe}{Mg}\right)_{Ol} = \frac{Mg^{2+} - 2}{Mg^{2+}}, \quad \text{(S-3)}$$

$$\text{moles } Mg^{2+} = \frac{2}{(1-(Fe/Mg)_{Ol})} \quad \text{and} \quad MgO_{Ol}\ (\text{wt. \%}) = \text{moles } Mg^{2+} \times 40.3, \quad \text{(S-4, S-5)}$$

$$Fe^{2+} = 2 - Mg^{2+} \quad \text{and} \quad FeO_{Ol}\ (\text{wt. \%}) = \text{moles } Fe^{2+} \times 71.8. \quad \text{(S-6, S-7)}$$

2) Calculate the new melt composition after olivine addition. For 1 % (0.01) incremental additions of olivine, this is given as:

$$FeO_{melt}^{new} = (1 - 0.01)FeO_{melt}^{previous} + (0.01)FeO_{Ol}, \quad \text{(S-8)}$$

$$MgO_{melt}^{new} = (1 - 0.01)MgO_{melt}^{previous} + (0.01)MgO_{Ol}. \quad \text{(S-9)}$$

3) Calculate the change in melt $\delta^{56}Fe$ following olivine addition. The proportion of Fe in olivine and melt is calculated as:

$$\Delta F(Fe) = (0.01) \times \frac{Fe_{Ol}}{Fe_{melt}}. \quad \text{(S-10)}$$

Then a mass balance equation is used to calculate the change in Fe isotopic composition of the melt:

$$\delta^{56}\mathrm{Fe_{Ol}} = \delta^{56}\mathrm{Fe_{melt}} + \Delta^{56}\mathrm{Fe_{Ol-melt}}, \quad \text{(S-11)}$$

$$\delta^{56}\mathrm{Fe_{melt}^{new}} = \big(1 - \Delta F(\mathrm{Fe})\big)\delta^{56}\mathrm{Fe_{melt}^{previous}} + \Delta F(\mathrm{Fe})\delta^{56}\mathrm{Fe_{Ol}}. \quad \text{(S-12)}$$

This is repeated incrementally until Mg# reaches 0.74 and olivine forsterite content reaches 90, which is assumed to represent a primary melt.

There are several different ways that $\Delta^{56}\mathrm{Fe_{Ol\text{-}melt}}$ can be calculated, which is a large source of uncertainty with the fractional crystallisation corrections. For this study, we used two separate methods:

- **Method 1:**

  From Sossi and O'Neill (2017), the olivine-melt fractionation factor can be expressed as:

  $$\Delta^{56}\mathrm{Fe_{Ol-melt}} = 2904 \times \frac{F_{\mathrm{Ol}} - F_{\mathrm{melt}}}{T^2}, \quad \text{(S-13)}$$

  where F_{Ol} has a value of 197 N/m (Dauphas *et al.*, 2014), F_{melt} varies depending on melt $\mathrm{Fe^{3+}/\Sigma Fe}$ but has a value of approximately 222 N/m when $\mathrm{Fe^{3+}/\Sigma Fe}$ is near 0.15 (since $F_{\mathrm{Fe^{2+}}}$ = 199 N/m and $F_{\mathrm{Fe^{3+}}}$ = 351 N/m; Dauphas *et al.*, 2014). Temperature is calculated using the expression from Nisbet (1982):

  $$T(\mathrm{K}) = [1000 + 20 \times \mathrm{MgO\ (wt.\%)}] + 273. \quad \text{(S-14)}$$

- **Method 2:**

  The maximum correction which has been proposed so far in the literature is $\Delta^{57}\mathrm{Fe_{Ol\text{-}melt}} = -0.4 \times 10^6/T^2$ (Nebel *et al.*, 2019) which is equivalent to $\Delta^{56}\mathrm{Fe_{Ol\text{-}melt}} = -0.276 \times 10^6/T^2$. We use this expression to calculate the maximum magnitude of possible fractional crystallisation correction.

For the Fagradalsfjall data, the corrected Fe isotopic compositions ($\delta^{56}\mathrm{Fe_{prim}}$) are shown in Figure S-1 by the red bars. Correction Method 1 gives a $\Delta^{56}\mathrm{Fe_{Ol\text{-}melt}}$ value of approximately −0.03 ‰, and a minimum δ^{56}Fe correction. We consider this to be a realistic correction because it is based on fractionation factors directly determined using NRIXS. Correction Method 2 gives a $\Delta^{56}\mathrm{Fe_{Ol\text{-}melt}}$ value of approximately −0.10 ‰, which we suspect may be an overcorrection of the data.

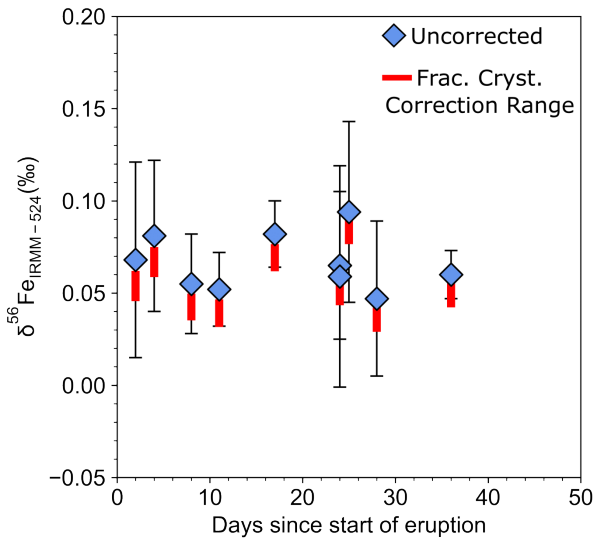

Figure S-1 Iron isotopic compositions of the Fagradalsfjall basalts corrected for olivine crystallisation. The red bar spans the range of the $\delta^{56}Fe_{prim}$ values calculated using two separate methods, as described in the text.

The Fagradalsfjall lavas are relatively primitive, with high Mg# between 64 and 67, and olivine cores with Fo content between 80 and 90 % (Halldórsson *et al.*, 2022), which suggests they have experienced limited fractional crystallisation. For both correction methods, the $\delta^{56}Fe_{prim}$ values are still within analytical uncertainty.

There are many uncertainties with fractional crystallisation corrections, the largest being which olivine-melt fractionation factors are selected. If different fractionation factors are chosen, discrepancies in the corrections are accentuated in those samples which have undergone the most olivine crystallisation. While this is less of an issue in the Fagradalsfjall samples, it becomes an increasingly important issue to consider in less primitive basalts, and those that crystallise phases other than olivine. In addition, there are uncertainties with assuming a $Fe^{3+}/\Sigma Fe$ for the melt, and in estimating accurate crystallisation temperatures.

For the above reasons, we chose to report and plot the uncorrected $\delta^{56}Fe$ values in this paper, as the correction had no effect on our Fe isotope trends or interpretations, and could instead increase uncertainty.

4. Fe Isotope Modelling During Mantle Melting

The variations in major and trace element composition in the Fagradalsfjall basalts is thought to be caused by changes in the proportions of melt contributed by depleted and enriched mantle domains over the course of the eruption, with melts from a geochemically enriched source becoming more significant with time (Halldórsson *et al.*, 2022). However, it is uncertain if this source is lithologically distinct (*i.e.* pyroxenitic). The aim of the Fe isotope modelling in this section is to investigate the source required to generate the trace element and Fe isotopic compositions of the Fagradalsfjall basalts.

We use a batch melting model after Sossi and O'Neill (2017) to model the trace element and Fe isotopic composition of melts produced from batch melting spinel lherzolite, garnet lherzolite, and pyroxenite sources (Fig. S-2). A full explanation of the calculations is given below. The parameters used are listed in Tables S-3 to S-6.

Batch Melting Models

Trace element concentrations in the melt (C_l) are calculated using a batch melting equation:

$$\frac{C_l}{C_o} = \frac{1}{(D+F(1-P))}. \qquad \text{(S-15)}$$

The Fe isotope modelling follows the approach outlined in Sossi and O'Neill (2017), and calculates the concentrations of the isotopes ^{54}Fe and ^{56}Fe in the melt (l). Equation S-16 is the general form of this equation, where i is the isotope being calculated, j denotes the normalising isotope (^{54}Fe), and C_o is the initial concentration in the bulk solid. F is the melt fraction, and is varied in steps of 0.02.

$$\frac{C_l^i}{C_o^i} = \frac{1}{\left(\left(D^j_{1-2}\alpha E^{\frac{i}{j}}_{1-2}\right)+F(1-P)\right)}. \qquad \text{(S-16)}$$

The term $\alpha E^{\frac{i}{j}}_{1-2}$ is the isotopic fractionation factor of element E, and is equivalent to the ratio of the two partition coefficients D^i_{1-2}/D^j_{1-2}. For example, Fe isotopes fractionation between the melt (l) and mantle (o) is expressed as:

$$\alpha \mathrm{Fe}^{\frac{56}{54}}_{l-o} = \frac{D^{56}_{l-o}}{D^{54}_{l-o}} = \frac{(^{56}\mathrm{Fe})_l\ /(^{56}\mathrm{Fe})_o}{(^{54}\mathrm{Fe})_l\ /(^{54}\mathrm{Fe})_o}. \qquad \text{(S-17)}$$

However, since at high temperatures, α is approximately equal to 1, the partition coefficients for D^j and D^i are approximately equal. It is assumed that the partition coefficient for the normalising isotope D^j (^{54}Fe) is equal to the bulk partition coefficient for Fe (see Sossi and O'Neill, 2017, for the full derivation). The partition coefficient for D^i (^{56}Fe) can then be calculated from Equation S-18, where K is the force constant of Fe-O bonds in the minerals and melt and x is a constant equal to 2904 which considers the difference in mass between the two isotopes (see Equation B-13 in Sossi and O'Neill, 2017, for the equation to calculate x):

$$D^{^{56}\mathrm{Fe}}_{\mathrm{min-melt}} = \left(D^{^{54}\mathrm{Fe}}_{\mathrm{min-melt}}\right) e^{\left(\frac{x\left(K^{\mathrm{min}}_{\mathrm{Fe-O}} - K^{\mathrm{melt}}_{\mathrm{Fe-O}}\right)}{T^2}\right)}. \qquad \text{(S-18)}$$

The force constants for the minerals are given in Tables S-4 to S-6, and remain constant throughout the model. We select force constants determined by the same method (NRIXS) for consistency. The force constant for the melt scales with melt $Fe^{3+}/\Sigma Fe$, and is calculated at each model step using Equation S-19, from the Dauphas *et al.* (2014) regression for force constants in basaltic, andesitic and dacitic glasses (a = 152 and b = 199):

$$K^{\mathrm{melt}}_{\mathrm{Fe-O}} = a \times \frac{\mathrm{Fe}^{3+}}{\Sigma\mathrm{Fe}} + b \qquad \text{(S-19)}$$

Therefore, for ^{56}Fe, Equation S-16 reduces to:

$$\frac{C_l^{56}}{C_o^{56}} = \frac{1}{\left(\left(D_{\text{min-melt}}^{56}\right)+F(1-P)\right)}, \qquad \text{(S-20)}$$

and for ^{54}Fe, Equation S-16 reduces to:

$$\frac{C_l^{54}}{C_o^{54}} = \frac{1}{\left(\left(D_{\text{min-melt}}^{54}\right)+F(1-P)\right)}. \qquad \text{(S-21)}$$

Dividing $\frac{C_l^{56}}{C_o^{56}}$ by $\frac{C_l^{54}}{C_o^{54}}$ gives the Fe isotope fractionation factor between the melt and the mantle ($\alpha Fe_{l-o}^{\frac{56}{54}}$; Eq. S-17). Therefore, the Fe isotopic composition of the melt can be calculated using Equation S-22, where $\delta^{56}Fe_o$ is the initial Fe isotopic composition of the mantle source.

$$\delta^{56}Fe_l = \delta^{56}Fe_o + 1000\ln\left(\frac{(^{56}Fe)_l\ /(^{56}Fe)_o}{(^{54}Fe)_l\ /(^{54}Fe)_o}\right) = \delta^{56}Fe_o + 1000\ln\left(\alpha Fe_{l-o}^{\frac{56}{54}}\right). \qquad \text{(S-22)}$$

Model Parameters

Table S-3 Initial Parameters for non-modal batch melting models for spinel peridotite, garnet peridotite and MORB-like pyroxenite.

Parameter	Spinel Peridotite	Reference	Garnet Peridotite	Reference	Pyroxenite	Reference
FeO (wt. %)	8.18	Workman and Hart (2005), DMM	8.18	Workman and Hart (2005), DMM	9.35	Lambart (2017), G2 pyroxenite
$Fe^{3+}/\Sigma Fe$	0.036	Sossi and O'Neill (2017), intermediate value	0.036	Sossi and O'Neill (2017), intermediate value	0.16	Cottrell and Kelley (2011), average MORB
$\delta^{56}Fe$	0.026	Craddock *et al.* (2013), DMM	0.026	Craddock *et al.* (2013), DMM	0.105	Teng *et al.* (2013), average MORB
La (µg/g)	0.192	Workman and Hart (2005), DMM	0.192	Workman and Hart (2005), DMM	2.695	Lambart (2017), G2 pyroxenite
Yb (µg/g)	0.365	Workman and Hart (2005), DMM	0.365	Workman and Hart (2005), DMM	3.4	Lambart (2017), G2 pyroxenite
Nb (µg/g)	0.1485	Workman and Hart (2005), DMM	0.1485	Workman and Hart (2005), DMM	6.13	Lambart (2017), G2 pyroxenite
Zr (µg/g)	5.082	Workman and Hart (2005), DMM	5.082	Workman and Hart (2005), DMM	65	Lambart (2017), G2 pyroxenite

Table S-4 Input parameters for melting a spinel-bearing depleted peridotite. Modal proportions are from Workman and Hart (2005). Melting coefficients are from Kinzler and Grove (1992). Partition coefficients for Fe^{2+} and Fe^{3+} are from Mallmann and O'Neill (2009). Trace element partition coefficients are from Gibson and Geist (2010). Force constants are from ([a]) Dauphas *et al.* (2014; forsterite value) and ([b]) Roskosz *et al.* (2015; median value for spinel). Due to the lack of NRIXS measurements for pyroxene, we assume olivine, orthopyroxene and clinopyroxene have equal force constants. In reality, Fe^{3+} bearing pyroxene will have a higher force constant than Fe^{2+} bearing olivine.

Mineral	Modal Proportion	Melting Coefficient	$D(Fe^{2+})$	$D(Fe^{3+})$	D(La)	D(Yb)	D(Nb)	D(Zr)	Force Constant (N/m)
olivine	0.57	−0.3	1.08	0.063	0.0005	0.02	0.0005	0.0033	197[a]
orthopyroxene	0.28	0.4	0.68	0.201	0.0031	0.08	0.004	0.013	197[a]
clinopyroxene	0.13	0.82	0.287	0.453	0.049	0.4	0.015	0.119	197[a]
spinel	0.02	0.08	1.93	2.88	0	0	0	0	264[b]

Table S-5 Input parameters for melting a garnet-bearing depleted peridotite. Modal proportions are from Hirschmann and Stolper (1996). Melting coefficients are from Walter (2003; garnet lherzolite at 3 GPa). Partition coefficients for Fe^{2+} and Fe^{3+} are from Mallmann and O'Neill (2009). Trace element partition coefficients are from Gibson and Geist (2010). The force constant for garnet is from Nie *et al.* (2021), and those for olivine and pyroxenes are as above.

Mineral	Modal Proportion	Melting Coefficient	$D(Fe^{2+})$	$D(Fe^{3+})$	D(La)	D(Yb)	D(Nb)	D(Zr)	Force Constant (N/m)
olivine	0.525	0.05	1.08	0.063	0.0005	0.02	0.0005	0.0033	197[a]
orthopyroxene	0.23	−0.15	0.68	0.201	0.0031	0.08	0.004	0.013	197[a]
clinopyroxene	0.175	0.96	0.287	0.453	0.049	0.4	0.015	0.119	197[a]
garnet	0.07	0.14	0.60	0.18	0.001	6.6	0.015	0.27	110

Table S-6 Input parameters for melting a MORB-like pyroxenite. Melting coefficients are from Pertermann and Hirschmann (2003). Modal proportions selected to represent an average pyroxenite. Partition coefficients for Fe^{2+} and Fe^{3+} for clinopyroxene are from Mallmann and O'Neill (2009), and assume that values are similar for garnet and orthopyroxene after Sossi and O'Neill (2017). Trace element partition coefficients are from Gibson and Geist (2010). The force constant for garnet is from Nie *et al.* (2021) and that for clinopyroxene is as above.

Mineral	Modal Proportion	Melting Coefficient	$D(Fe^{2+})$	$D(Fe^{3+})$	D(La)	D(Yb)	D(Nb)	D(Zr)	Force Constant (N/m)
clinopyroxene	0.8	0.872	0.287	0.453	0.049	0.4	0.015	0.119	197
garnet	0.2	0.173	0.60	0.18	0.001	6.6	0.015	0.27	110

Modelling Results

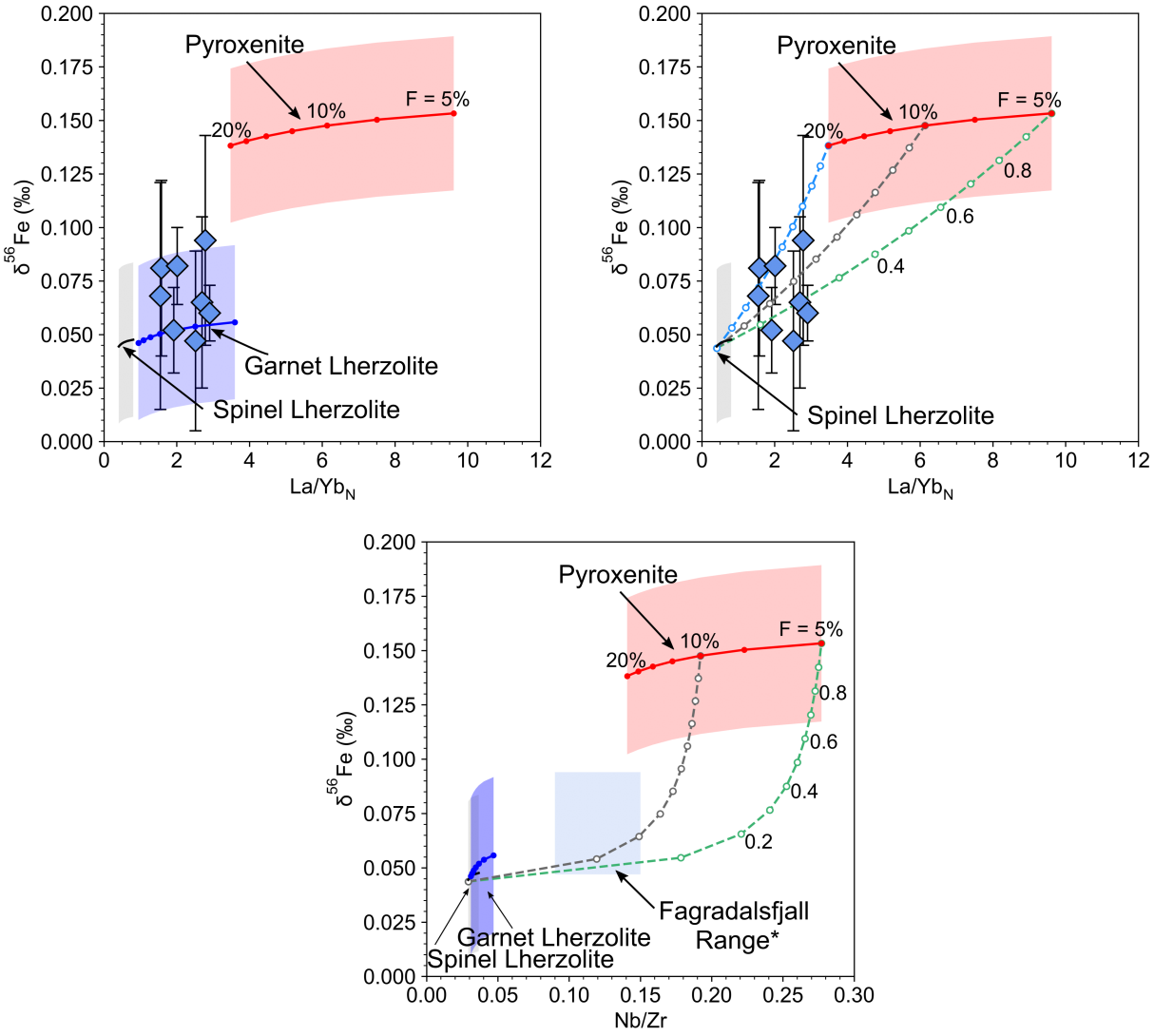

Figure S-2 Batch melting models of trace element and Fe isotopic composition, and binary mixing between end-member melts. La and Yb data are from Halldórsson *et al.* (2022). The Nb and Zr data for the Fagradalsfjall samples are for a different sample set from Bindeman *et al.* (2022), so are shown as a range.

Figure S-2 shows that if melting occurs within the spinel stability field, a minor proportion (~10–20 %) of pyroxenite melt is required to explain the La/Yb ratios of the lavas. However, if melting is >3 GPa and garnet is present in the mantle source, melting a garnet bearing peridotite at different pressures and melt fractions can explain the range of La/Yb and δ^{56}Fe in the Fagradalsfjall lavas. However, in order to explain the Nb/Zr ratios of the lavas (as reported in Bindeman *et al.*, 2022), a minor pyroxenite contribution (~10–20 % pyroxenite melt) is required. However, such a low proportion of pyroxenite does not cause resolvable variations in the major element or Fe isotopic composition of the melt.

In order to investigate the proportion and Fe isotopic composition of enriched end member melts which are required to cause a resolvable variation in basalt Fe isotopic composition, we construct a simple binary mixing model

using Equation S-23, where p is the proportion of end member A. For simplicity, the FeO content of the end member melts is assumed to be equal, although in reality this will vary with depth and degree of melting:

$$\delta^{56}Fe_{melt} = \frac{p*FeO_A*\delta^{56}Fe_A + (1-p)*FeO_B*\delta^{56}Fe_B}{p*FeO_A + (1-p)*FeO_B}. \quad \text{(S-23)}$$

Assuming a spinel lherzolite has initial δ^{56}Fe similar to the depleted MORB mantle (0.026 ‰; Craddock *et al.*, 2013), a depleted melt would have δ^{56}Fe ≈ 0.05 ‰ (*e.g.*, see Fig. S-2). For the enriched melt, if a pyroxenite source has initial δ^{56}Fe similar to average MORB (0.105 ‰; Teng *et al.*, 2013), the melt would have δ^{56}Fe ≈ 0.150 ‰ (*e.g.*, see Fig. S-2). However, pyroxenite xenoliths with δ^{56}Fe up to 0.20 ‰ have been measured previously (Zhao *et al.*, 2017). If the bulk melt-mantle fractionation factor is approximately 0.04–0.06 ‰ during pyroxenite melting, then a melt with δ^{56}Fe ≈ 0.25 ‰ could hypothetically be produced.

In reality, enriched melts are not sourced directly from the melting of subducted ocean crust. Instead, silica rich melts sourced from melting of recycled crust react with the peridotite mantle, consuming olivine and orthopyroxene and forming a hybrid source containing pyroxenite. Soderman *et al.* (2021) propose melts from reaction zone pyroxenites could be as heavy as δ^{57}Fe = 0.30 ‰ (or δ^{56}Fe ≈ 0.2 ‰), although these are likely rare heavy values. Therefore, we use a geologically feasible range of enriched end member compositions from 0.10 ‰ to 0.25 ‰.

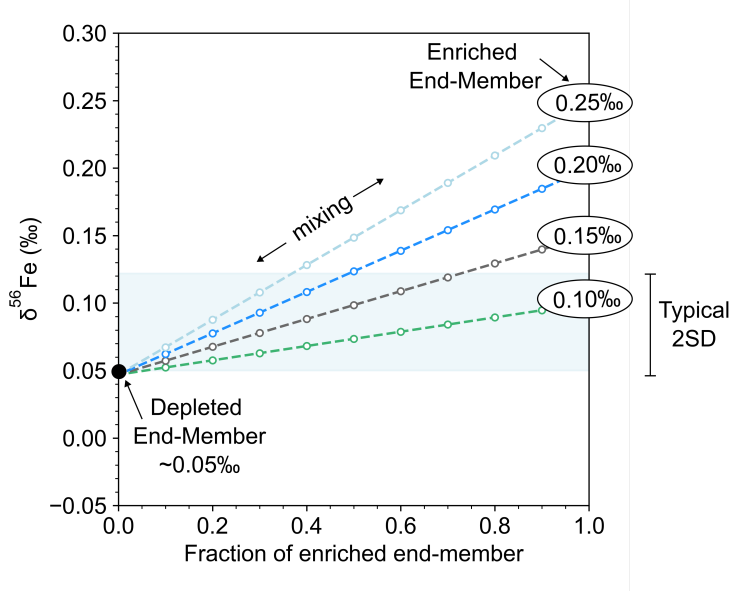

Figure S-3 Binary mixing model of depleted and enriched end members. The blue shaded area is the typical analytical uncertainty of Fe isotope measurements, which here is the average 2 s.d. measured in this study. Values for the depleted and enriched end members are discussed in the text.

The binary mixing model (Fig. S-3) shows that at current analytical uncertainty, at least 40–50 % enriched melt with δ^{56}Fe > 0.2 ‰ is generally required to generate resolvable Fe isotopic variation. This therefore suggests that at Fagradalsfjall there is no significant contribution of melts from a lithologically distinct (pyroxenite) mantle component, or the melting signal of enriched lithologies is masked by more significant peridotite melting.

Additional Figures

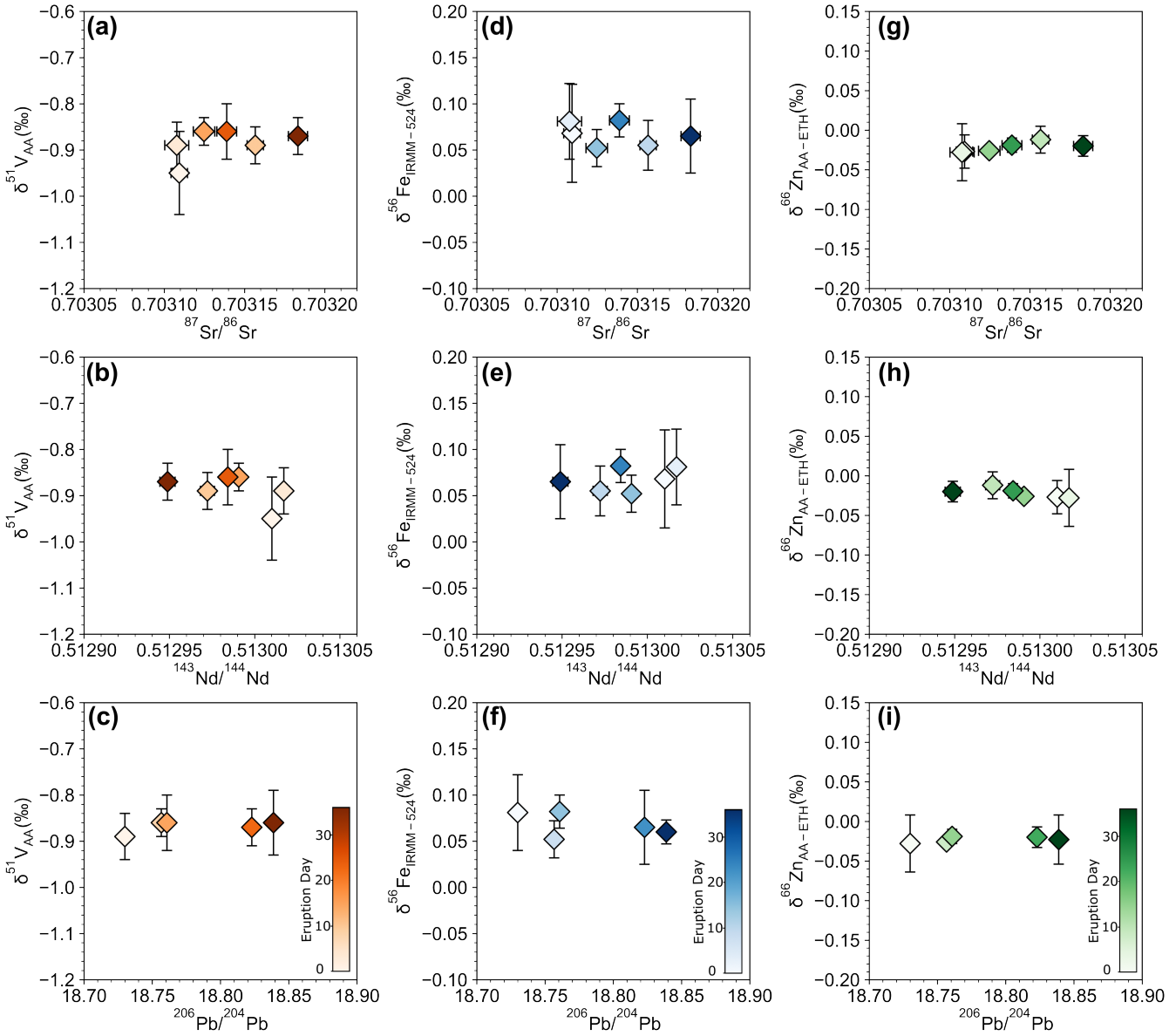

Figure S-4 Whole rock **(a–c)** vanadium, **(d–f)** iron and **(g–i)** zinc isotopic compositions plotted against **(a, d, g)** $^{87}Sr/^{86}Sr$, **(b, e, h)** $^{143}Nd/^{144}Nd$ and **(c, f, i)** $^{206}Pb/^{204}Pb$ from Halldórsson *et al.* (2022). The colour bars indicate the day the samples were erupted.

Supplementary Information References

Archer, C., Andersen, M.B., Cloquet, C., Conway, T.M., Dong, S., Ellwood, M., Moore, R., Nelson, J., Rehkämper, M., Rouxel, O., Samanta, M., Shin, K.-C., Sohrin, Y., Takano, S., Wasylenki, L. (2017) Inter-calibration of a proposed new primary reference standard AA-ETH Zn for zinc isotopic analysis. *Journal of Analytical Atomic Spectrometry* 32, 415–419. https://doi.org/10.1039/C6JA00282J

Bindeman, I.N., Deegan, F.M., Troll, V.R., Thordarson, T., Höskuldsson, Á., Moreland, W.M., Zorn, E.U., Shevchenko, A.V., Walter, T.R. (2022) Diverse mantle components with invariant oxygen isotopes in the 2021 Fagradalsfjall eruption, Iceland. *Nature Communications* 13, 3737. https://doi.org/10.1038/s41467-022-31348-7

Cottrell, E., Kelley, K.A. (2011) The oxidation state of Fe in MORB glasses and the oxygen fugacity of the upper mantle. *Earth and Planetary Science Letters* 305, 270–282. https://doi.org/10.1016/j.epsl.2011.03.014

Craddock, P.R., Dauphas, N. (2011) Iron Isotopic Compositions of Geological Reference Materials and Chondrites. *Geostandards and Geoanalytical Research* 35, 101–123. https://doi.org/10.1111/j.1751-908X.2010.00085.x

Craddock, P.R., Warren, J.M., Dauphas, N. (2013) Abyssal peridotites reveal the near-chondritic Fe isotopic composition of the Earth. *Earth and Planetary Science Letters* 365, 63–76. https://doi.org/10.1016/j.epsl.2013.01.011

Dauphas, N., Roskosz, M., Alp, E.E., Neuville, D.R., Hu, M.Y., Sio, C.K., Tissot, F.L.H., Zhao, J., Tissandier, L., Médard, E., Cordier, C. (2014) Magma redox and structural controls on iron isotope variations in Earth's mantle and crust. *Earth and Planetary Science Letters* 398, 127–140. https://doi.org/10.1016/j.epsl.2014.04.033

Gibson, S.A., Geist, D. (2010) Geochemical and geophysical estimates of lithological thickness variation beneath Galápagos. *Earth and Planetary Science Letters* 300, 275–286. https://doi.org/10.1016/j.epsl.2010.10.002

Gong, H., Guo, P., Chen, S., Duan, M., Sun, P., Wang, X., Niu, Y. (2020) A re-assessment of nickel-doping method in iron isotope analysis on rock samples using multi-collector inductively coupled plasma mass spectrometry. *Acta Geochimica* 39, 355–364. https://doi.org/10.1007/s11631-019-00392-4

Halldórsson, S.A., Marshall, E.W., Caracciolo, A., Matthews, S., Bali, E., Rasmussen, M.B., Ranta, E., Robin, J.G., Guðfinnsson, G.H., Sigmarsson, O., Maclennan, J., Jackson, M.G., Whitehouse, M.J., Jeon, H., van der Meer, Q.H.A., Mibei, G.K., Kalliokoski, M.H., Repczynska, M.M., Rúnarsdóttir, R.H., Sigurðsson, G., Pfeffer, M.A., Scott, S.W., Kjartansdóttir, R., Kleine, B.I., Oppenheimer, C., Aiuppa, A., Ilyinskaya, E., Bitetto, M., Giudice, G., Stefánsson, A. (2022) Rapid shifting of a deep magmatic source at Fagradalsfjall volcano, Iceland. *Nature* 609, 529–534. https://doi.org/10.1038/s41586-022-04981-x

Hirschmann, M.M., Stolper, E.M. (1996) A possible role for garnet pyroxenite in the origin of the "garnet signature" in MORB. *Contributions to Mineralogy and Petrology* 124, 185–208. https://doi.org/10.1007/s004100050184

Kinzler, R.J., Grove, T.L. (1992) Primary magmas of mid-ocean ridge basalts 1. Experiments and methods. *Journal of Geophysical Research: Solid Earth* 97, 6885–6906. https://doi.org/10.1029/91JB02840

Lambart, S. (2017) No direct contribution of recycled crust in Icelandic basalts. *Geochemical Perspectives Letters* 4, 7–12. https://doi.org/10.7185/geochemlet.1728

Mallmann, G., O'Neill, H.St.C. (2009) The Crystal/Melt Partitioning of V during Mantle Melting as a Function of Oxygen Fugacity Compared with some other Elements (Al, P, Ca, Sc, Ti, Cr, Fe, Ga, Y, Zr and Nb). *Journal of Petrology* 50, 1765–1794. https://doi.org/10.1093/petrology/egp053

Maréchal, C.N., Télouk, P., Albarède, F. (1999) Precise analysis of copper and zinc isotopic compositions by plasma-source mass spectrometry. *Chemical Geology* 156, 251–273. https://doi.org/10.1016/S0009-2541(98)00191-0

Nie, N.X., Dauphas, N., Alp, E.E., Zeng, H., Sio, C.K., Hu, J.Y., Chen, X., Aarons, S.M., Zhang, Z., Tian, H.-C., Wang, D., Prissel, K.B., Greer, J., Bi, W., Hu, M.Y., Zhao, J., Shahar, A., Roskosz, M., Teng, F.-Z., Krawczynski, M.J., Heck, P.R., Spear, F.S. (2021)

Iron, magnesium, and titanium isotopic fractionations between garnet, ilmenite, fayalite, biotite, and tourmaline: Results from NRIXS, *ab initio*, and study of mineral separates from the Moosilauke metapelite. *Geochimica et Cosmochimica Acta* 302, 18–45. https://doi.org/10.1016/j.gca.2021.03.014

Nielsen, S.G., Prytulak, J., Halliday, A.N. (2011) Determination of Precise and Accurate $^{51}V/^{50}V$ Isotope Ratios by MC-ICP-MS, Part 1: Chemical Separation of Vanadium and Mass Spectrometric Protocols. *Geostandards and Geoanalytical Research.* 35, 293–306. https://doi.org/10.1111/j.1751-908X.2011.00106.x

Nisbet, E.G. (1982). The tectonic setting and petrogenesis of komatiites. In: Arndt, N.T., Nisbet, E.G. (Eds.) *Komatiites*. Allen & Unwin, London, 501–520.

Nebel, O., Sossi, P.A., Bénard, A., Arculus, R.J., Yaxley, G.M., Woodhead, J.D., Davies, D.R., Ruttor, S. (2019) Reconciling petrological and isotopic mixing mechanisms in the Pitcairn mantle plume using stable Fe isotopes. *Earth and Planetary Science Letters* 521, 60–67. https://doi.org/10.1016/j.epsl.2019.05.037

Pertermann, M., Hirschmann, M.M. (2003) Anhydrous Partial Melting Experiments on MORB-like Eclogite: Phase Relations, Phase Compositions and Mineral-Melt Partitioning of Major Elements at 2–3 GPa. *Journal of Petrology* 44, 2173–2201. https://doi.org/10.1093/petrology/egg074

Roeder, P.L., Emslie, R.F. (1970) Olivine-liquid equilibrium. *Contributions to Mineralogy and Petrology* 29, 275–289. https://doi.org/10.1007/BF00371276

Roskosz, M., Sio, C.K.I., Dauphas, N., Bi, W., Tissot, F.L.H., Hu, M.Y., Zhao, J., Alp, E.E. (2015) Spinel-olivine-pyroxene equilibrium iron isotopic fractionation and applications to natural peridotites. *Geochimica et Cosmochimica Acta* 169, 184–199. https://doi.org/10.1016/j.gca.2015.07.035

Soderman, C.R., Matthews, S., Shorttle, O., Jackson, M.G., Ruttor, S., Nebel, O., Turner, S., Beier, C., Millet, M.-A., Widom, E., Humayun, M., Williams, H.M. (2021) Heavy $\delta^{57}Fe$ in ocean island basalts: A non-unique signature of processes and source lithologies in the mantle. *Geochimica et Cosmochimica Acta* 292, 309–332. https://doi.org/10.1016/j.gca.2020.09.033

Sossi, P.A., O'Neill, H.St.C. (2017) The effect of bonding environment on iron isotope fractionation between minerals at high temperature. *Geochimica et Cosmochimica Acta* 196, 121–143. https://doi.org/10.1016/j.gca.2016.09.017

Sossi, P.A., Halverson, G.P., Nebel, O., Eggins, S.M. (2015) Combined Separation of Cu, Fe and Zn from Rock Matrices and Improved Analytical Protocols for Stable Isotope Determination. *Geostandards and Geoanalytical Research* 39, 129–149. https://doi.org/10.1111/j.1751-908X.2014.00298.x

Sossi, P.A., Nebel, O., Foden, J. (2016) Iron isotope systematics in planetary reservoirs. *Earth and Planetary Science Letters* 452, 295–308. https://doi.org/10.1016/j.epsl.2016.07.032

Teng, F.-Z., Dauphas, N., Huang, S., Marty, B. (2013) Iron isotopic systematics of oceanic basalts. *Geochimica et Cosmochimica Acta* 107, 12–26. https://doi.org/10.1016/j.gca.2012.12.027

Walter, M.J. (2003) 2.08 - Melt Extraction and Compositional Variability in Mantle Lithosphere. In: Holland, H.D., Turekian, K.K. (Eds.) *Treatise on Geochemistry*. First Edition, Elsevier, Amsterdam, 363–394. https://doi.org/10.1016/B0-08-043751-6/02008-9

Workman, R.K., Hart, S.R. (2005) Major and trace element composition of the depleted MORB mantle (DMM). *Earth and Planetary Science Letters* 231, 53–72. https://doi.org/10.1016/j.epsl.2004.12.005

Wu, F., Qi, Y., Yu, H., Tian, S., Hou, Z., Huang, F. (2016) Vanadium isotope measurement by MC-ICP-MS. *Chemical Geology* 421, 17–25. https://doi.org/10.1016/j.chemgeo.2015.11.027

Zhao, X.M., Cao, H.H., Mi, X., Evans, N.J., Qi, Y.H., Huang, F., Zhang, H.F. (2017) Combined iron and magnesium isotope geochemistry of pyroxenite xenoliths from Hannuoba, North China Craton: implications for mantle metasomatism. *Contributions to Mineralogy and Petrology* 172, 40. https://doi.org/10.1007/s00410-017-1356-y